Kovove Mater. 62 2024 285–293
DOI: 10.31577/km.2024.5.285

An LSTM-PSO model for forecasting the flow behavior of a Ni-based superalloy during hot deformation

Guo-Chuan Pan[1], Bai-Wei Zhou[1], Wang Li[2,3], Chang-Xu Chen[1], Wei-Wei Zhao[2,3], Guan-Qiang Wang[4]*, Ming-Song Chen[5]**, Yong-Cheng Lin[4]

[1] *Zhejiang Zheneng Yueqing Electric Power Generation Co., Ltd, Wenzhou 325609, P. R. China*
[2] *Zhejiang Energy Technology Research Institute Co., Ltd, Hangzhou 311121, P. R. China*
[3] *Zhejiang Key Laboratory of Thermal Power Generation Energy Efficiency and Pollutant Control Technology, Hangzhou 311121, P. R. China*
[4] *School of Mechanical and Electrical Engineering, Central South University, Changsha 410083, P. R. China*
[5] *Light Alloy Research Institute of Central South University, Changsha 410083, P. R. China*

Received 10 September 2024, received in revised form 24 October 2024, accepted 25 October 2024

Abstract

Isothermal compressive experiments on a Ni-based superalloy were performed at strain rates from 0.001 to 1 s^{-1} and temperatures between 920 and 1040 ℃ to study its high--temperature deformation. Utilizing the experimental data, a Long Short-Term Memory (LSTM) model, optimized with the Particle Swarm Optimization (PSO) algorithm (LSTM--PSO), was developed to characterize this behavior. The LSTM component of the model effectively handles the complexity and nonlinear characteristics of time-series data, while the PSO component performs parameter optimization, enhancing the model's accuracy and generalization capability. The model's inputs include deformation temperature, strain rate, and true strain, with true stress as the output. A comparison of experimental and forecasted results revealed that the LSTM-PSO model accurately predicts high-temperature deformation, achieving a correction coefficient of 0.9988 and an average absolute relative error of 1.16, demonstrating superior performance compared to other advanced methods.

K e y w o r d s: hot deformation, Ni-based superalloy, Long Short-Term Memory (LSTM) method, Particle Swarm Optimization (PSO) algorithm, constitutive model

1. Introduction

Ni-based superalloys are extensively employed in essential components of aerospace engines and gas turbines due to their superior mechanical characteristics and excellent resistance to corrosion and oxidation [1–3]. These components are commonly produced through hot die forging. However, the deformation behavior of Ni-based superalloys at high temperatures is highly complex [4–6]. Many researchers have conducted studies focusing on model development to understand better and predict the thermal manufacturing process of these alloys, progressively uncovering the mechanisms of microstructure evolution during hot deformation [7–9]. Processing maps for Ni-based superalloys have been developed to assess power dissipation efficiency, identify regions of flow instability, and optimize hot working conditions [10, 11]. Investigations into the dynamic recrystallization (DRX) behavior of these alloys [12–14] have led to the establishment of precise phenomenological and physically based constitutive models for predicting high-temperature flow stress [15–17]. Jiang et al. [18] introduced a cellular automaton model [19] to simulate grain growth in a powder metallurgy Ni-based superalloy. Zhang et al. [20] and Lin et al. [21] explored interactions between recrystallization and the precipitation/dissolution behavior of the δ phase, finding that the δ phase promotes DRX nucleation during hot deformation of Inconel 718 and GH4169 superalloy. Furthermore, meta-dynamic recrystallization (MDRX) behavior was investigated in a Ni-Cr-Mo al-

*Corresponding author: e-mail address: wgq001101@gmail.com
**Corresponding author: e-mail address: chenms18@csu.edu.cn

loy, developing accurate MDRX kinetic and grain size models [22].

Previous research has documented various metallurgical phenomena that occur during the hot manufacturing of Ni-based alloys [23, 24]. There is growing interest in constitutive models capable of accurately forecasting material rheology by integrating phenomenology, physical mechanisms, or intelligent methodologies [25]. Based on empirical observations, phenomenological constitutive models have been devised to precisely forecast the true stresses of metals [26–28]. Nevertheless, the above models frequently lack a strong physical basis [29]. Conversely, physically based constitutive models offer a detailed characterization of deformation mechanisms across a broad parameter range based on specific physical assumptions [30–32]. However, the intricate and nonlinear nature of high-temperature deformation behavior in alloys poses challenges for accurate true stress predictions. Intelligent models, including neural networks [33], genetic algorithms [34], deep belief networks [35], and reasoning systems [36], are proven effective in accurately characterizing thermal deformation behavior under complex conditions [37]. These models do not depend on specific mathematical formulas and can be easily developed using experimental data. Furthermore, leveraging its continuous learning capability, the long short-term memory (LSTM) method excels in creating precise input-output data mappings. Consequently, LSTM has been effectively used to forecast the true stress of composites and alloys [38, 39].

Despite extensive research on hot deformation behavior and microstructure evolution of typical superalloys, current constitutive models are still insufficiently advanced. This study conducted isothermal compressive experiments at various temperatures and strain rates to examine the high-temperature deformation of a Ni-based superalloy. An optimized Long Short-Term Memory (LSTM) model, enhanced with the Particle Swarm Optimization (PSO) algorithm (LSTM-PSO), was developed to characterize the alloy's high-temperature deformation. The predictive performance of the LSTM-PSO model was validated by comparing it with both phenomenological and physically based models.

2. Experiments preparation

For this research, we used the same materials and preparation methods as those described in the author's previous research [40]. The original microstructure before deformation, demonstrated in Fig. 1, features equiaxed grains with an average size of 73 μm. Isothermal compressive experiments were carried out on Gleeble-3500 at strain rates ranging from 0.001 to 1 s^{-1} and deformation temperatures between 920 and 1040 ℃, resulting in a 70 % reduction in specimen height.

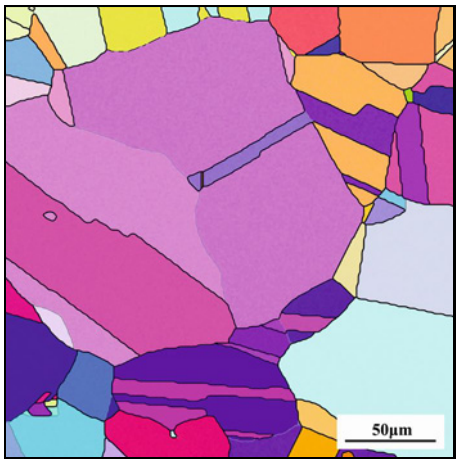

Fig. 1. Original microstructure of the superalloy under investigation.

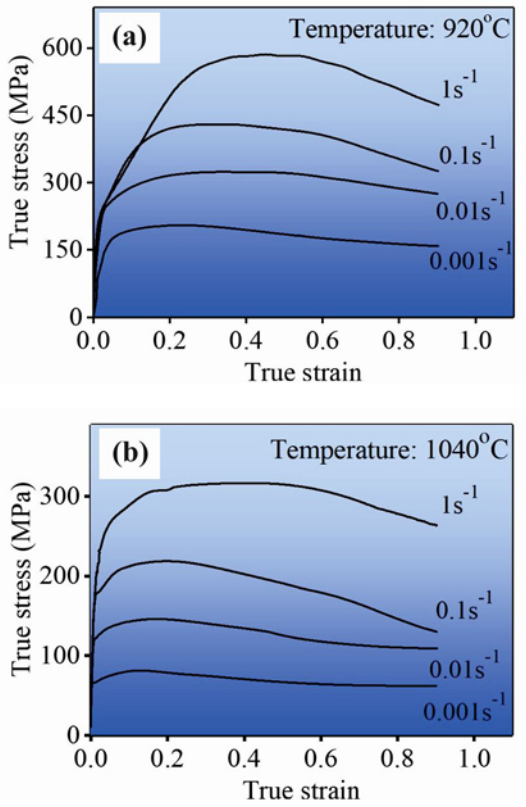

Fig. 2. Observed true stress-strain (TSS) curves for the superalloy under investigation at diverse temperatures: (a) 920 ℃ and (b) 1040 ℃ [40].

As illustrated in Fig. 2, it is noteworthy that the true stress decreases with rising temperatures. Additionally, higher strain rates generally lead to increased true stress. The reason for this behavior can be sum-

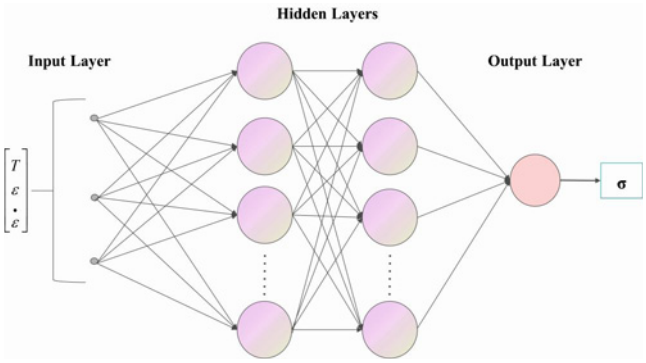

Fig. 3. Typical structure network of LSTM model.

marized as follows: when the strain rate is low, more time is provided for dynamic recrystallization (DRX) behavior and supporting various dislocation movements [41, 42].

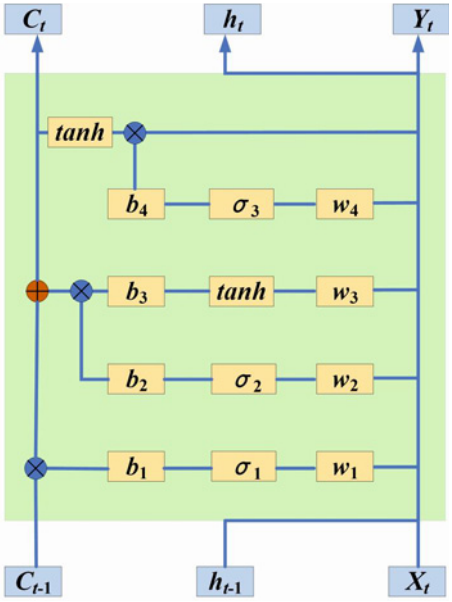

Fig. 4. Data transmission within an LSTM unit.

3. Development of an LSTM-PSO model for forecasting true stress

In this work, the LSTM, known for its capability to forecast nonlinear stress-strain curves, is applied to analyze the thermal compression behavior of the Ni-based alloy under investigation. The typical architecture of the LSTM model includes input layers comprising variables T, ε, and $\dot{\varepsilon}$, with the output layer defined as σ, as depicted in Fig. 3. Based on the report in [43] regarding the unique characteristics of thermal stress-strain data for Ni-based superalloys, the same 2 hidden layers in the LSTM model are applied.

The LSTM model typically uses gradient descent to find the global optimal solution, as illustrated in Fig. 4. Forgetting gate, inputting gate, and outputting gate are used to protect and control the cell state to learn or forget information from time series data. Specifically, the forgetting gate eliminates irrelevant input data from the last cell state by [44]:

$$f_t = \sigma_1 \left(W_\mathrm{f} \left[h_{t-1}, x_t \right] + b_1 \right). \tag{1}$$

Subsequently, the status of each cell is determined. In this process, the sigmoid function (σ_i) of the input gate is used for activation, deciding which information needs to be updated. This information is then passed on to the hyperbolic tangent activation function (tanh) for further processing. The formulae for i_t and $\tilde{C}$ are expressed as follows [45]:

$$i_t = \sigma_2 \left(W_\mathrm{i} \left[h_{t-1}, x_t \right] + b_2 \right), \tag{2}$$

$$\tilde{C} = \tanh \left(W_\mathrm{c} \left[h_{t-1}, x_t \right] + b_3 \right). \tag{3}$$

Moreover, the input and forget gates are merged, leading to an update in the cell state from C_{t-1} to C_t. The update equation for C_t is formulated as [45]:

$$C_t = f_t C_{t-1} + i_t \tilde{C}_t. \tag{4}$$

Therefore, the information processed by the output gate o_t is updated by [45]:

$$o_t = \sigma_3 \left(W_\mathrm{o} \left[h_{t-1}, x_t \right] + b_4 \right). \tag{5}$$

Eventually, by disposing of the activation function (tanh), the subsequent hidden state of the output gate is determined as [44]:

$$h_t = o_t \tanh \left(C_t \right), \tag{6}$$

where W_o, W_f, W_i, and W_c denote the weights of the output gate, forget gate, input gate, and candidate gate, respectively. b_1, b_2, b_3, and b_4 are the biases of the output gate, forget gate, input gate, and candidate gate, respectively. $[h_{t-1}, x_t]$ represents the input data.

It is normally known that the LSTM model can effectively overcome the defects of vanishing gradients and exploding gradients. However, several characteristics, including susceptibility to falling into local minima and the relatively limited convergence rate, significantly affect the applicability of the LSTM model. To improve the convergence speed and forecast accuracy of the LSTM model, the PSO algorithm coupling with the LSTM model (LSTM-PSO) is proposed to reconstruct the thermal compression behavior. The PSO algorithm is commonly characterized as an evolutionary computing technology based on swarm intel-

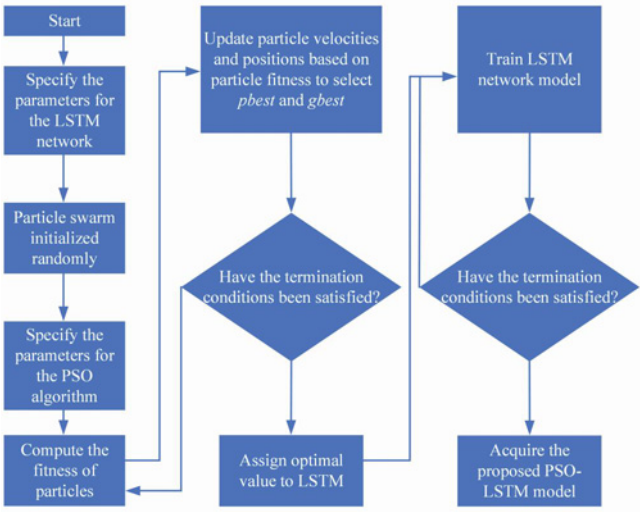

Fig. 5. Flowchart illustrating the PSO-optimized LSTM neural network.

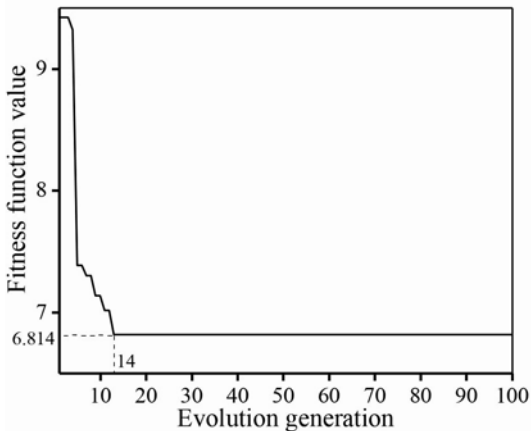

Fig. 6. Training process of the PSO-LSTM algorithm.

ligence. The PSO algorithm updates individual positions by tracking the individual extreme value (*pbest*) and group best (*gbest*) values. Equations (7) and (8) governing particle velocity and position are shown below [44]:

$$\nu_{\mathrm{i}} = W \times \nu_{\mathrm{i}} + c_1 \times rand\,() \times (pbest_{\mathrm{i}} - x_{\mathrm{i}}) + c_2 \times rand\,() \times (gbest_{\mathrm{i}} - x_{\mathrm{i}})\,, \tag{7}$$

$$x_{\mathrm{i}} = x_{\mathrm{i}} + v_{\mathrm{i}}, \tag{8}$$

where v_{i} denotes particle speed, W describes the inertia factor, c_1 and c_2 are learning indexes, *rand*() represents a random number between 0 and 1, and x_{i} depicts the present location of the particles.

Figure 5 illustrates the flow chart of the PSO--optimized LSTM neural network [46]. The parameters for the LSTM network and the PSO algorithm are initially set. Next, the fitness function, which evaluates the root mean square error (RMSE) between forecasted and actual values, is established. Simultaneously, the individual best value (*pbest*) and the group best value (*gbest*) are updated based on fitness evaluations. The optimal outcomes are then utilized in the LSTM model, followed by training to achieve the final LSTM model results.

The experimental data is segmented into 24 sets, with 18 sets allocated for training and the remaining 6 sets for model validation. Compliant with the developed LSTM network, the PSO particle matrix has a length of 6 [46], representing the number of nodes in the two hidden layers. The population size is fixed at 14, with a learning factor of 4, and a maximum iteration step of 120.

During the LSTM model training, a total of 1200 iterations are completed with a mini-batch size of 128. Moreover, a gradient threshold of 1 is defined, and the training process utilizes the Adaptive Moment Estimation (Adam) method. To facilitate a seamless training process, the model's data is normalized:

$$X = \frac{X - X_{\min}}{X_{\max} - X_{\min}}, \tag{9}$$

where X denotes the input value, and $X_{\min}$ and $X_{\max}$ represent the maximum and minimum values, respectively.

Following data input, the PSO-LSTM model performs iterative calculations to reach convergence, which is evaluated using a fitness function. Generally, the smaller values indicate better convergence. As shown in Fig. 6, the 14th iteration, the best particle's fitness value stabilizes at its lowest point (6.814). Consequently, optimal LSTM parameters are determined: 280 nodes in hidden layer 1, 140 nodes in hidden layer 2, 186 nodes in the fully connected layer, and a learning rate 0.018. These parameters are used in the LSTM model to forecast flow stress.

4. Discussion

To evaluate the prediction accuracy of the LSTM-PSO model, we performed detailed comparisons between experimental results and those forecasted by the LSTM-PSO model, as well as other advanced constitutive models. Similar to [40], we computed the correction coefficient (R) and average absolute relative error ($AARE$) for the true stresses observed versus those forecasted.

Aside from the established LSTM-PSO model based on machine learning, constitutive models are categorized into two types: physically based and strain-compensated phenomenological models. Therefore, models from these categories applicable to the

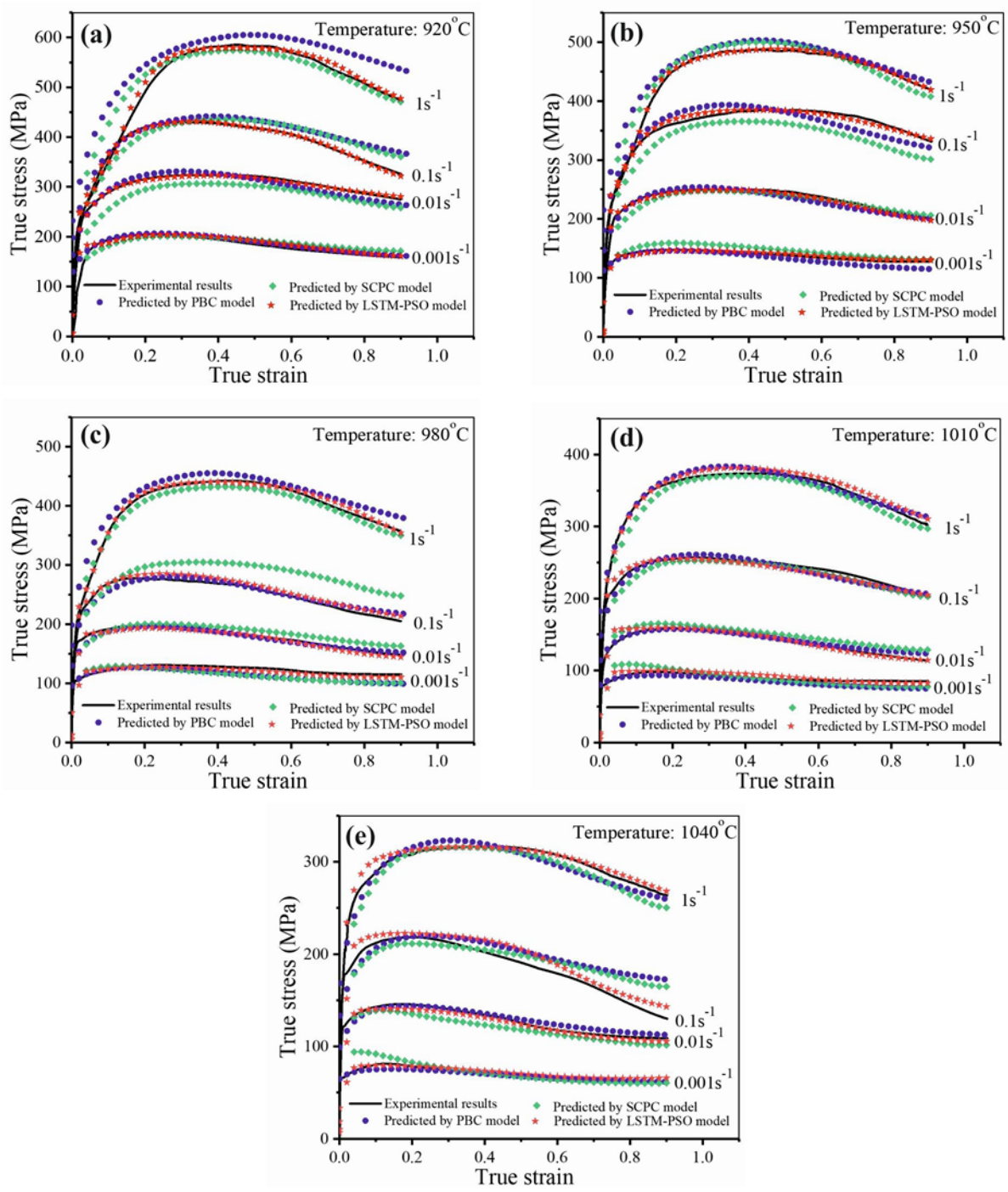

Fig. 7. Comparative analysis of forecasted and observed TSS curves for the Ni-based superalloy under diverse deformation temperatures: (a) 920 °C, (b) 950 °C, (c) 980 °C, (d) 1010 °C, and (e) 1040 °C.

studied material or similar materials were selected for comparative analysis in this research.

(a) Physically based constitutive (PBC) model

The PBC model [30] can be written as follows:

$$\sigma = \left[\sigma_{\text{sat}}^2 + \left(\sigma_0^2 - \sigma_{\text{sat}}^2\right) \mathrm{e}^{-\Omega\varepsilon}\right]^{0.5} \quad (\varepsilon < \varepsilon_{\text{c}})$$

$$\sigma = \sigma_{\text{rec}} - \left(\sigma_{\text{sat}} - \sigma_{\text{ss}}\right) \cdot \left\{1 - \exp\left[-K_{\text{d}}\left(\frac{\varepsilon - \varepsilon_{\text{c}}}{\varepsilon_{\text{p}}}\right)^{1.85}\right]\right\} \quad (\varepsilon \geq \varepsilon_{\text{c}})$$

$$\sigma_{\text{rec}} = \left[\sigma_{\text{sat}}^2 + \left(\sigma_0^2 - \sigma_{\text{sat}}^2\right) \mathrm{e}^{-\Omega\varepsilon}\right]^{0.5}$$

$$\sigma_{\text{sat}} = -11.30 + 1.07\sigma_{\text{p}}$$

$$\sigma_0 = 14.86 \ln Z - 478.07$$

$$\Omega = 2344.39Z^{-0.12208}$$
$$\sigma_{ss} = 0.74925\sigma_p$$
$$\varepsilon_p = 0.00188Z^{0.11741}$$
$$\varepsilon_c = 0.00160Z^{0.11741}$$
$$K_d = 0.00033Z^{0.16103}$$
$$Z = \dot{\varepsilon}\exp\left(4.74\times10^5/8.31T\right) \quad (13)$$

where σ_{sat} and σ_{ss} represent the saturation and steady stresses, respectively, σ_{rec} denotes the flow stress when dynamic recovery is the primary softening mechanism. ε demonstrates the true strain, while ε_c indicates the critical strain for initiating dynamic recrystallization, σ_0 denotes the yield stress, Ω represents the coefficient of dynamic recovery. ε_p refers to the absolute temperature (K), and Z stands for the Zener-Hollomon parameter.

(b) Strain-compensated phenomenological constitutive (SCPC) model

The SCPC model [26] can be described by Eq. (14). It incorporates additional parameters compared to the PBC model, t, α, n, ln A, and Q represent material constants, and V represents the original δ phase content. In this study, V is set to 0.

As depicted in Fig. 7, the true stresses forecasted by the LSTM-PSO model are more accurate than those for the other three models.

$$\sigma = \frac{1}{\alpha}\ln\left(\left(\frac{Z}{A}\right)^{1/n} + \left(\left(\frac{Z}{A}\right)^{2/n} + 1\right)^{1/2}\right)$$
$$Z = \dot{\varepsilon}\exp\left[Q/\left(RT\right)\right]n$$
$$\alpha = \left\{[6.604, -4.635, -0.006]\,[1, \varepsilon, V]^{\mathrm{T}} + [\varepsilon, V]\begin{pmatrix} 9.492 - 4.559\varepsilon 0.202 + 0.148\varepsilon \\ 0.202 + 0.005V - 0.025 + 0.001V \end{pmatrix}\cdot [\varepsilon, V]^{\mathrm{T}}\right\} \times 10^{-3}$$
$$n = [3.475, 0.941, 0.204]\,[1, \varepsilon, V]^{\mathrm{T}} + [\varepsilon, V]\begin{pmatrix} 1.815 - 9.699\varepsilon 0.202 + 0.489\varepsilon \\ -0.131 + 0.010V - 0.018 + 0.0004V \end{pmatrix}[\varepsilon, V]^{\mathrm{T}}$$
$$\ln A = [33.559, -4.965, -2.009]\,[1, \varepsilon, V]^{\mathrm{T}} + [\varepsilon, V]\begin{pmatrix} 8.855 + 21.349\varepsilon 2.466 - 6.805\varepsilon \\ 2.466 - 0.394\mathrm{V}0.660 - 0.039V \end{pmatrix}[\varepsilon, V]^{\mathrm{T}}$$
$$Q = [412.647, -61.455, -21.299]\,[1, \varepsilon, V]^{\mathrm{T}} + [\varepsilon, V]\cdot\begin{pmatrix} 127.928 + 167.934\varepsilon 27.795 - 75.833\varepsilon \\ 27.795 - 4.320\mathrm{V}6.896 - 0.404V \end{pmatrix}[\varepsilon, V]^{\mathrm{T}} \quad (14)$$

Significant errors in forecasted stress are observed for the PBC and SCPC models at high strain rates (1 and 0.1 s^{-1}), attributed to the overestimate of the work-hardening behavior [47]. Furthermore, the comparison of predicted and observed true stresses is depicted in Fig. 8, showcasing the superior predictive accuracy of the LSTM-PSO model. A side-by-side evaluation of the predictive performance between the LSTM-PSO model and the other three models is detailed in Table 1, which includes R and $AARE$ values. The R for the PBC, SCPC, and LSTM-PSO models are 0.9870, 0.9904, and 0.9988, respectively, indicating a strong correlation between forecasted and observed results. Moreover, the $AARE$ of the LSTM-PSO model is 1.16 %, significantly lower than that for the other three models, highlighting the higher prediction accuracy of the LSTM-PSO model. Consequently, the LSTM-PSO model provides a more precise description of the high-temperature deformation behavior of the Ni-based superalloy studied.

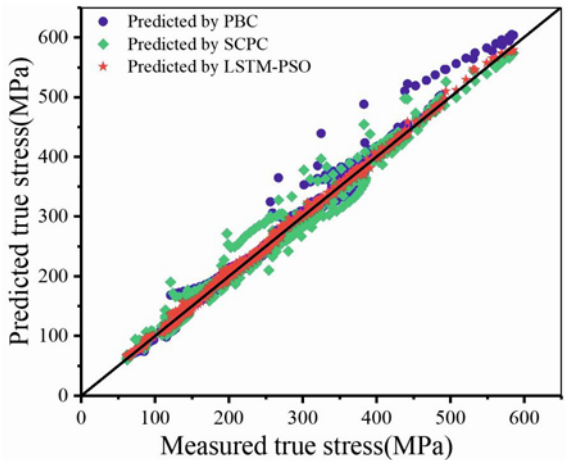

Fig. 8. Correlation between the observed and forecasted true stresses.

Table 1. Evolution indexes of PBC, SCPC and LSTM--PSO models

Method	R	$AARE$ (%)
PBC	0.9870	2.93
SCPC	0.9904	2.38
LSTM-PSO	0.9988	1.16

Typically, in predicting material properties, due to the significant relationship between these properties and physical phenomena such as phase transitions, models developed based on the underlying laws and mechanisms tend to perform comparably to advanced deep learning methods that do not account for fundamental physical changes. In this study, the LSTM-PSO approach demonstrates distinct performance advantages primarily due to the following factors: (1) PSO can automatically optimize the hyperparameters of LSTM, thereby enhancing its learning capability and enabling more efficient capture of key information in the stress-strain curve; (2) when external conditions or input data change, PSO dynamically adjusts

model parameters, improving the model's adaptability and robustness, allowing for more accurate predictions of stress-strain behavior under varying materials and temperature conditions; (3) PSO's parameter optimization reduces the complexity of the LSTM model, enabling more precise selection of key parameters and thereby improving overall performance.

5. Conclusions

In this study, a Long Short-Term Memory (LSTM) model cooperating with the Particle Swarm Optimization (PSO) algorithm (LSTM-PSO) was established to analyze the deformation flow behavior of the Ni-based superalloy. The LSTM-PSO model can accurately forecast true stress at deformation temperatures between 920 and 1040 ℃ and strain rates from 0.001 to 1 s^{-1}. With a correction coefficient of 0.9988 and an average absolute relative error of 1.16, the LSTM-PSO model demonstrates superior predictive performance compared to conventional physically based and phenomenological models. This is due to its ability to effectively handle the complexity and nonlinear characteristics of time-series data while optimizing parameters to improve model accuracy and generalization. The application of this method facilitates more precise material property predictions, providing strong support for material design and engineering applications.

Acknowledgements

This work was supported by the National Key Research and Development Program of China under Grant 2022YFB3706901.

This work was also supported by Zhejiang Energy Group Science and Technology Program (ZNKJ-2022-005). The authors gratefully acknowledge Zhejiang Energy Group Co., Ltd.,Zhejiang Zheneng Yueqing Electric Power Generation Co., Ltd and Zhejiang Energy Technology Research Institute Co., Ltd., for utilization of all the facilities and resources.

References

[1] G. Q. Wang, M. S. Chen, Y. C. Lin, H. B. Li, Y. Q. Jiang, Y. Q. Ma, C. X. Peng, J. L. Cai, Q. Chen, Recrystallization nucleation under close-set 8 phase in a nickel-based superalloy during annealing, J. Mater. Sci. Technol. 115 (2022) 166–176. https://doi.org/10.1016/j.jmst.2021.11.016

[2] G. Q. Wang, M. S. Chen, H. B. Li, Y. C. Lin, W. D. Zeng, Y. Y. Ma, Methods and mechanisms for uniformly refining deformed mixed and coarse grains inside a solution-treated Ni-based superalloy by two-stage heat treatment, J. Mater. Sci. Technol. 77 (2021) 47–57. https://doi.org/10.1016/j.jmst.2020.11.030

[3] G. Q. Wang, M. S. Chen, Y. C. Lin, H. B. Li, W. D. Zeng, Y. Y. Ma, J. L. Cai, C. X. Peng, F. Y. Zou, A novel annealing method to uniformly refine deformed mixed grain microstructure of a solution-treated Ni-based superalloy, Sci. China-Technol. Sci. 64 (2021) 1741–1751. https://doi.org/10.1007/s11431-020-1784-x

[4] X. M. Chen, M. T. Ning, H. W. Hu, Y. C. Lin, X. J. Zhou, J. Zhang, X. Z. Lu, J. Chen, Y. X. Liu, Characterization of hot deformation behavior and optimization of hot workability for GH4698 superalloy, Mater. Charact. 201 (2023) 112916. https://doi.org/10.1016/j.matchar.2023.112916

[5] G. Q. Wang, H. B. Li, M. S. Chen, Y. C. Lin, W. D. Zeng, Y. Y. Ma, Q. Chen, Y. Q. Jiang, Effect of initial mixed grain microstructure state of deformed Ni-based superalloy on its refinement behavior during two-stage annealing treatment, Mater. Charact. 176 (2021) 111130. https://doi.org/10.1016/j.matchar.2021.111130

[6] D. G. He, Y. C. Lin, L. X. Yin, Creep characteristics and fracture mechanisms of a Ni-based superalloy with δ phases at intermediate temperatures, Adv. Eng. Mater. 22 (2020) 2000144. https://doi.org/10.1002/adem.202000144

[7] M. J. Sohrabi, A. Kalhor, H. Mirzadeh, K. Rodak, H. S. Kim, Tailoring the strengthening mechanisms of high-entropy alloys toward excellent strength-ductility synergy by metalloid silicon alloying: A review, Prog. Mater. Sci. 144 (2024) 101295. https://doi.org/10.1016/j.pmatsci.2024.101295

[8] F. Chen, X. Tian, G. S. Wu, H. J. Zhu, H. A. Ou, Z. S. Cui, Coupled quantitative modeling of microstructural evolution and plastic flow during continuous dynamic recrystallization, Int. J. Plast. 156 (2022) 103372. https://doi.org/10.1016/j.ijplas.2022.103372

[9] J. Zhao, G. Z. Quan, Y. Q. Zhang, W. Xiong, Distribution and evolution of low-energy twin boundary density in the time-space domain during isothermal compression for Ni80A superalloy, Trans. Nonferrous Met. Soc. China 33 (2023) 3387–3405. https://doi.org/10.1016/S1003-6326(23)66341

[10] S. L. Guo, S. S. Wu, J. T. Guo, Y. Z. Shen, W. Zhang, An investigation on the hot deformation behavior and processing maps of Co-Ni-Cr-W-based superalloy, J. Manuf. Process. 74 (2022) 100–111. https://doi.org/10.1016/j.jmapro.2021.11.060

[11] L. Chen, B. Zhang, Y. Yang, T. L. Zhao, Y. Xu, Q. Wang, B. Zan, J. Cai, K. Wang, X. Chen, Evolution of hot processing map and microstructure of as-forged nickel-based superalloy during hot deformation, J. Mater. Res. Technol. – JMRT 24 (2023) 7638–7653. https://doi.org/10.1016/j.jmrt.2023.05.060

[12] A. Momeni, G. R. Ebrahimi, M. Jahazi, H. R. Ezatpour, Microstructure characterization and dynamic recrystallization behavior of Ni-Cu alloy during hot deformation, Mech. Mater. 193 (2024) 105002. https://doi.org/10.1016/j.mechmat.2024.105002

[13] M. H. Marzbali, H. R. Jafarian, S. Bokaei, N. Park, A. Momeni, A. R. Eivani, On the microstructure and mechanical properties of FeCoCrCuNi high entropy alloy during hot compression, J. Mater. Res. Technol. – JMRT 16 (2022) 1747–1760. https://doi.org/10.1016/j.jmrt.2021.12.019

[14] H. Yu, Z. T. Wang, Y. Q. Ning, S. Huang, Q. M. Liu, DRX mechanisms of a Ni-Co-W type superalloy with typical columnar grains during hot compression, J. Alloy. Compd. 959 (2023) 170533. https://doi.org/10.1016/j.jallcom.2023.170533
[15] X. P. Cao, S. Z. Zhang, C. J. Zhang, S. L. Zhang, Y. F. Chen, Q. B. Wang, X. Cheng, Model selection and stress prediction of Ti-45Al-9Nb alloy during hot deformation, Kovove Mater. 58 (2020) 13–24. https://doi.org/10.4149/km_2020_1_13
[16] Y. S. Fan, L. Tan, X. G. Yang, D. Q. Shi, R. Z. Li, J. Huang, C. Wang, A microstructural rafting state-based constitutive model for single crystal Ni-based superalloys at elevated temperature, Int. J. Mech. Sci. 228 (2022) 107484. https://doi.org/10.1016/j.ijmecsci.2022.107484
[17] Y. C. Zhu, Z. Q. Huang, J. X. Fan, L. Qin, Y. Niu, Study of high-temperature deformation behavior and thermal processing diagram of cast TA15 titanium alloy, Kovove Mater. 61 (2023) 369–383. https://doi.org/10.31577/km.2023.6.369
[18] Y. L. Jiang, S. S. Liu, R. G. Lu, X. Cheng, J. Li, Y. Chen, G. F. Tian, Cellular automata simulation of grain growth of powder metallurgy Ni-based superalloy, J. Iron Steel Res. Int. 30 (2023) 838–848. https://doi.org/10.1007/s42243-023-00921-9
[19] H. J. Zhu, F. Chen, H. M. Zhang, Z. S. Cui, Review on modeling and simulation of microstructure evolution during dynamic recrystallization using cellular automaton method, Sci. China-Technol. Sci. 63 (2020) 357–396. https://doi.org/10.1007/s11431-019-9548-x
[20] F. X. Zhang, D. Liu, Y. H. Yang, C. X. Liu, J. G. Wang, Z. Zhang, H. P. Wang, Investigation on the influences of δ phase on the dynamic recrystallization of Inconel 718 through a modified cellular automaton model, J. Alloy. Compd. 830 (2020) 154590. https://doi.org/10.1016/j.jallcom.2020.154590
[21] Y. C. Lin, D. G. He, M. S. Chen, X. M. Chen, C. Y. Zhao, X. Ma, Z. L. Long, EBSD analysis of evolution of dynamic recrystallization grains and δ phase in a nickel-based superalloy during hot compressive deformation, Mater. Des. 97 (2016) 13–24. https://doi.org/10.1016/j.matdes.2016.02.052
[22] D. G. He, X. T. Yan, Y. C. Lin, Y. C. Xia, Microstructural evolution and kinetic characteristics during metadynamic recrystallization in a Ni-Cr-Mo alloy, J. Alloy. Compd. 926 (2022) 166830. https://doi.org/10.1016/j.jallcom.2022.166830
[23] B. C. Xie, B. Y. Zhang, Y. Q. Ning, M. W. Fu, Mechanisms of DRX nucleation with grain boundary bulging and subgrain rotation during the hot working of nickel-based superalloys with columnar grains, J. Alloy. Compd. 786 (2019) 636–647. https://doi.org/10.1016/j.jallcom.2019.01.334
[24] E. Eriksson, F. Hanning, J. Andersson, M. H. Colliander, Dynamic recrystallization during hot compression of Ni-based superalloy Haynes 282, J. Alloy. Compd. 960 (2023) 170837. https://doi.org/10.1016/j.jallcom.2023.170837
[25] K. A. Babu, T. S. Prithiv, A. Gupta, S. Mandal, Modeling and simulation of dynamic recrystallization in super austenitic stainless steel employing combined cellular automaton, artificial neural network and finite element method, Comput. Mater. Sci. 195 (2021) 110482. https://doi.org/10.1016/j.commatsci.2021.110482
[26] Y. C. Lin, M. He, M. S. Chen, D. X. Wen, J. Chen, Effects of initial δ phase (Ni3Nb) on hot tensile deformation behaviors and material constants of Ni-based superalloy, Trans. Nonferrous Met. Soc. China 26 (2016) 107–117. https://doi.org/10.1016/S1003-6326(15)64043-2
[27] S. Gupta, C. A. Bronkhorst, Crystal plasticity model for single crystal Ni-based superalloys: Capturing orientation and temperature dependence of flow stress, Int. J. Plast. 137 (2021) 102896. https://doi.org/10.1016/j.ijplas.2020.102896
[28] X. M. Chen, L. Y. Nie, H. W. Hu, Y. C. Lin, J. Zhang, X. J. Zhou, X. Z. Lu, J. Chen, Y. X. Liu, Investigation on the fracture mechanism and constitutive relations of a typical Ni-based superalloy, Mater. Today Commun. 35 (2023) 105612. https://doi.org/10.1016/j.mtcomm.2023.105612
[29] D. He, X. T. Yan, Y. C. Lin, S. Zhang, Z. J. Chen, Microstructure evolution and constitutive model for a Ni-Mo-Cr base alloy in double-stages hot compression with step-strain rates, Mater. Charact. 194 (2022) 112385. https://doi.org/10.1016/j.matchar.2022.112385
[30] Y. C. Lin, X. M. Chen, D. X. Wen, M. S. Chen, A physically-based constitutive model for a typical nickel-based superalloy, Comput. Mater. Sci. 83 (2014) 282–289. https://doi.org/10.1016/j.commatsci.2013.11.003
[31] Z. J. Chen, Y. C. Lin, D. G. He, Y. M. Lou, M. S. Chen, A unified dislocation density-based model for an aged polycrystalline Ni-based superalloy considering the coupled effects of complicate deformation mechanisms and initial δ phase, Mater. Sci. Eng. A-Struct. Mater. Prop. Microstruct. Process. 827 (2021) 142062. https://doi.org/10.1016/j.msea.2021.142062
[32] X. M. Chen, L. Y. Nie, H. W. Hu, Y. C. Lin, Y. X. Liu, Z. L. Wu, X. J. Zhou, J. Zhang, X. Z. Lu, High-temperature deformation characteristics and constitutive models of Inconel 625 superalloy, Mater. Today Commun. 32 (2022) 103855. https://doi.org/10.1016/j.mtcomm.2022.103855
[33] J. F. Fatriansyah, I. Suhariadi, H. A. Fauziyyah, I. R. Syukran, F. Hartoyo, D. Dhaneswara, Z. Lockman, A. Fauzi, M. S. Rohman, Prediction and optimization of mechanical properties of Ni based and Fe-Ni based super alloys via neural network approach with alloying composition parameter, J. Mater. Res. Technol. – JMRT 24 (2023) 4168–4176. https://doi.org/10.1016/j.jmrt.2023.04.065
[34] B. Xu, H. Q. Yin, X. Jiang, C. Zhang, R. J. Zhang, Y. W. Wang, X. H. Qu, Z. H. Deng, G. Q. Yang, D. F. Khan, Data-driven design of Ni-based turbine disc superalloys to improve yield strength, J. Mater. Sci. Technol. 155 (2023) 175–191. https://doi.org/10.1016/j.jmst.2023.01.032
[35] F. Yang, W. Y. Zhao, Y. Ru, Y. L. Pei, S. S. Li, S. K. Gong, H. B. Xu, Deep learning accelerates the development of Ni-based single crystal superalloys: A physical-constrained neural network for creep rupture life prediction, Mater. Des. 232 (2023) 112174. https://doi.org/10.1016/j.matdes.2023.112174

[36] Y. D. Zhang, G. J. Xiao, J. Ma, H. Gao, B. Zhu, Y. Huang, A hybrid approach of process reasoning and artificial intelligence-based intelligent decision system framework for fatigue life of belt grinding, Int. J. Adv. Manuf. Technol. 130 (2023) 311–328. https://doi.org/10.1007/s00170-023-12597-2
[37] D. X. Wen, T. Y. Yue, Y. B. Xiong, K. Wang, J. K. Wang, Z. Z. Zheng, J. J. Li, High-temperature tensile characteristics and constitutive models of ultrahigh strength steel, Mater. Sci. Eng. A-Struct. Mater. Prop. Microstruct. Process. 803 (2021) 140491. https://doi.org/10.1016/j.msea.2020.140491
[38] H. Mei, L. H. Lang, X. G. Yang, Z. Liu, X. X. Li, Study on constitutive relation of nickel-base superalloy Inconel 718 based on long short term memory recurrent neural network, Metals 10 (2020) 1588. https://doi.org/10.3390/met10121588
[39] D. W. Li, J. X. Liu, W. Q. Huang, Z. X. Zuo, Y. Shi, W. J. Bai, Machine learning-based prediction for time series damage evolution of Ni-based superalloy microstructures, Mater. Today Commun. 33 (2022) 104533. https://doi.org/10.1016/j.mtcomm.2022.104533
[40] D. D. Chen, Y. C. Lin, Y. Zhou, M. S. Chen, D. X. Wen, Dislocation substructures evolution and an adaptive-network-based fuzzy inference system model for constitutive behavior of a Ni-based superalloy during hot deformation, J. Alloy. Compd. 708 (2017) 938–946. https://doi.org/10.1016/j.jallcom.2017.03.029
[41] J. F. Xiao, H. T. Cui, H. J. Zhang, W. D. Wen, J. Zhou, A physical-based constitutive model considering the motion of dislocation for Ni3Al-base superalloy, Mater. Sci. Eng. A Struct. Mater. Prop. Microstruct. Process. 772 (2020) 138631. https://doi.org/10.1016/j.msea.2019.138631
[42] H. Yu, W. Xu, S. van der Zwaag, Microstructure and dislocation structure evolution during creep life of Ni-based single crystal superalloys, J. Mater. Sci. Technol. 45 (2020) 207–214. https://doi.org/10.1016/j.jmst.2019.11.028
[43] H. N. Wen, S. L. Wang, J. S. Jin, X. Y. Wang, X. F. Tang, Y. D. Zhang, L. Deng, P. Gong, D. Li, B. Ning, Q. Wei, Deep learning-based modeling of the strain rate-dependent thermomechanical processing response for a novel HIPed P/M nickel-based superalloy, J. Mater. Process. Technol. 324 (2024) 118226. https://doi.org/10.1016/j.jmatprotec.2023.118226
[44] S. Xue, H. L. Chen, X. L. Zheng, Detection and quantification of anomalies in communication networks based on LSTM-ARIMA combined model, Int. J. Mach. Learn. Cybern. 13 (2022) 3159–3172. https://doi.org/10.1007/s13042-022-01586-8
[45] D. G. He, S. B. Chen, Y. C. Lin, H. Xie, C. B. Li, Hot tensile behavior of a 7046-aluminum alloy: Fracture mechanisms and constitutive models, Mater. Today Commun. 34 (2023) 105209. https://doi.org/10.1016/j.mtcomm.2022.105209
[46] D. G. He, S. B. Chen, Y. C. Lin, X. T. Yan, G. Liu, Hot deformation behavior of Hastelloy C276 alloy: Microstructural variation and constitutive models, Materials 16 (2023) 6192. https://doi.org/10.3390/ma16186192
[47] R. G. Ding, C. Knaggs, H. Y. Li, Y. G. Li, P. Bowen, Characterization of plastic deformation induced by machining in a Ni-based superalloy, Mater. Sci. Eng. A Struct. Mater. Prop. Microstruct. Process. 778 (2020) 139104. https://doi.org/10.1016/j.msea.2020.139104